Growth, Single crystal investigations, Hirshfeld surface analysis, DFT studies, Molecular Dynamics Simulations, Molecular docking, physico-chemical characterization and biological activity of novel thiocyanic complex with Zinc transition metal precursor

Jawher Makhlouf [a], Youness El Bakri[b,*], Arto Valkonen [c], Kandasamy Saravanan [d], Sajjad Ahmad[e] and Wajda Smirani [a,*]

a- Labortory of Material Chemistry, Faculty of Sciences of Bizerte, University of Carthage, Bizerte Zarzouna, Tunisia

b- Department of Theoretical and Applied Chemistry, South Ural State University, Lenin prospect 76, Chelyabinsk, 454080, Russian Federation.

c- Department of Chemistry, University of Jyvaskyla, 40014 Jyvaskyla, Finland

d- Faculty of Chemistry, University of Warsaw, Poland.

e- Department of Health and Biological Sciences, Abasyn University, Peshawar 25000, Pakistan.

Corresponding author: wajda_sta@yahoo.fr / yns.elbakri@gmail.com

Abstract

The present work undertakes the study of novel thiocyanic complex, which have been obtained due to the interaction of cationic entities with the thiocyanate ligands. In fact, these latter are added to a transition metal leading to the production of novel solid-state complex that was studied and characterized by single crystal X-ray crystallography. However, $(C_{11}H_{18}N_2O)[Zn(SCN)_4]$ crystallizes in orthorhombic system with the non-centrosymmetric space group $P\,2_12_12_1$, with the following lattice parameters: a=8.4726(2) Å , b=14.6043 (7) Å , c= 17.1927 (14) Å with V =2127.3 (14) $Å^3$ and Z = 4. Infrared spectrum was registered to revel the vibrational modes of the compound, add to the study of the optical properties using a polar solvent to carry out the UV–visible analysis. Thermogravimetric analysis techniques (TGA) and thermo-differential analysis techniques (DTA) were carried out to account for the thermal decomposition of complex. Furthermore, the antibacterial properties were determined against some bacteria. In order to gain insights into the role of weak molecular interactions in the complex that influence the self-assembly process and crystal packing, Hirshfeld surface analysis and DFT calculation were also performed. Furthermore, molecular docking and molecular dynamic simulations were performed for the compound against different antibacterial targets to identify to which target the compound show the best binding affinity. The MurF enzyme, which catalyzed the last cytoplasmic step of bacterial peptidoglycan synthesis, among the target was revealed to show better interactions with the enzyme and formed strong and stable intermolecular complex.

Keywords: Metal, Thiocyanate, Crystal structure, Antibacterial activities, DFT calculations, Molecular docking, Molecular dynamics simulation.

1. Introduction

Coordination compounds based on transition metal thiocyanates have occurred an increasing progress and interest in the last few years due to several reasons. First of all, the thiocyanate anion is a versatile ligand that can coordinate to metal cations in different ways leading to a large structural variety for the compounds **[1-4].** Moreover, this ligand is able to mediate a magnetic and electric exchange that can be used to prepare novel compounds that, depend on the nature of the metal cations and the topology of the coordination network, showing different properties **[5-7].** That is why, we gave much interest to this class of compounds. In the course of these investigations, we have also obtained several interesting isomeric and polymorphic modifications as for the case of chemical composition where all changes in the properties of the compounds can directly be correlated with their structures. This procedure often leads not only to the formation of metastable modifications but also to compounds with condensed thiocyanate networks **[8-9].** The synthesis of coordination compounds by solid state synthesis is considered as unusual something as well as other approaches are reported **[10-12].**

Nowadays, a huge interest is bringing to the coordination compounds. Among this large family, the main focus was on the hybrid compounds based on thiocyanates due to its huge application field. In particular, this work aims to investigate the interaction of 1-(2-metoxyphenyl) piperazine with Zinc (II) and thiocyanate ions according to two procedures which are; the liquid phase and the solid state.

According to recent research **[13-17],** terminal thiocyanate coordination is more well- known than bridge coordination. In view of these particular properties, the presence of thiocyanate

ligand makes the final coordination compound, which predict to obtain, added to the presence of zinc as transition metals, a solid-state compound.

The Hirshfeld surface analysis has been performed to completely characterize the intermolecular interactions and explain the crystalline architecture. In addition, the Zn complex was investigated by various spectroscopic studies. DFT calculations, Nonlinear optical properties, Natural bond and orbital analysis have been performed for the investigation of the interesting properties of the titled complex. Additionally, virtual screening of the compound against multiple antibacterial targets was performed to investigate the best binding receptors. This was achieved using molecular docking, followed by molecular dynamics simulations and binding free energy analysis. These methods are well known for identifying best binding molecules to receptors and discriminate between strong and weak binders.

2. Material and methods

2.1. Preparation of metal complex

2.1.1. Reagents

All materials were used as they were received without further purification. The amine 1-(2-Methoxyphenyl) piperazine and $ZnCl_2.6H_2O$ were obtained from Aldrich Chemical add to thiocyanate solution (HSCN) which was obtained from a cationic resin. All other solvents for synthesis and analysis were commercially available.

2.1.2. Preparation method

The solid metal complex was prepared by mixing 0.3 g of 1-(2 methoxyphenyl) piperazine dissolved in 25 mL and 25 mL of an aqueous solution of $ZnCl_2.6H_2O$, both dissolved in ethanol and stirred together. The thiocynic acid solution (HSCN), which is obtained from a

cationic resin (Amberlite IR- 120), exchange H-SO_3 using KSCN which added dropwise and well stirred.

The final colorless mixture was left to evaporate for a week at ambient temperature. The solid was filtered, washed using a mixture of water and ethanol and finally stored.

Elemental analysis for $(C_{11}H_{18}N_2O)[Zn(SCN)4]$ (491.96 g mol^{-1}): Anal. Calc. C, 46.03; H, 5.17; N, 22.69; S, 17.63% Found: C, 45.91; H, 4.91; N,21.42; S, 16.32%

Table1: Crystallographic data and structure refinement.

Chemical Formula:	$(C_{11}H_{18}N_2O)$ [Zn $(SCN)_4$]
Mr ($g.mol^{-1}$)	491.96
Crystal System:	Orthorhombic
Space Group:	P 2_1 2_1 2_1
A, b, c, (Å)	8.4726 (2), 14.6043 (7), 17.1927 (7)
β (°)	90
V ($Å^3$)	2127.36 (14)
Z	4
D ($g.cm^{-3}$)	1.536
F(000)	1008
R(reflexions)	2627
h,k,lmax	7,11, 22
Température (K):	170
Rdiation lenght MoKα (Å)	0.71073
Diffractometer:	bruker Kappa CCD
Thêta (max) (°) :	27.9
Mesurement rang : h, k, l :	−11 7, −19 11, −14 22
Number of independent reflexions :	4941
Used programs:	WinGx **[17]**
Direct Methods:	SHELX **[16]**
Reliability factor:	R = 0.043
	WR2=0.081
GooF = S :	1.07

Avec $w= 1/[\sigma^2(F_o^2) + (0.0651P)^2 + 0.3854P]$ où $P = (F_0^2 + 2F_c^2) /3$

2.2. X-ray crystallography

Single crystal X ray diffraction measurement was carried out on an automated four circle diffractometer (Bruker-Nonius Kappa CCD, diffractometer), containing a monochromatized-mirror using a graphite-monochromated MoKα (λ= 0.71073 Å) as radiation at 170 K. The structure was solved and reined on F^2 with the direct methods using the SHELXL software **[18]** incorporated in the wingX program package **[19].** A summary of Crystal data and experimental details are illustrated in **Table 1.**

2.3. Physical measurement

In order to characterize the obtained compound, physical measurement had been taken such as:

- The UV-Visible spectrum was recorded at room temperature by a Perkin Elmer Lambada 11 type spectrometer is used for the solid state.
- A Perkin Elmer Lambda spectrophotometer was used to record the electronic absorption spectrum in the range 700–220 cm^{-1} for the liquid state.
- FT-IR spectra of the formed complex was recorded using the spectrum of Perkin Elmer FT-IR between 400 and 4000 cm^{-1} which is performed in KBr pellets.
- The TGA/DTA thermograms were recorded by differential scanning to identify the thermal behavior. The product was placed into platinum pans heated up 500°C with a 5°C/min step in argon flow used as inert gas

2.4. Antibacterial material and methods

A suspension of the tested microorganisms was spread on the appropriate solid media plates and incubated overnight at 37°C. After one day, 4-5 loops of pure colonies were transferred to saline solution in a test tube for each bacterial strain and adjusted to the 0.5 McFarland

turbidity standard (~108 cells/mL). Sterile cotton was dipped into the bacterial suspension and the agar plates were streaked three times. Each time the plate was turning at a 60° angle and finally rubbing the swab through the edge of the plate. Sterile paper discs (Glass Microfiber filters, Whatman; 6 mm in diameter) were placed onto inoculated plates and impregnated with the diluted solutions in sterile water. Ampicillin (10µg/disc) was used as positive control for all strains except Candida albicans for which Nystatin (100µg/disc) was used. Inoculated plates with discs were placed in a 37 °C incubator. After 24 hours of incubation, the results were recorded by measuring the zones of growth inhibition surrounding the disc. Thus, clear inhibition zones around the discs indicated the presence of antimicrobial activity. The test was run in duplicates.

2.5. Molecular docking

The complex was drawn in ChemDraw ultra 12.0 **[20],** and energy minimized using MM2 force field **[21]**. Then, the complex was converted into ".pdb" format. Simultaneously, different antibacterial targets such DNA (pdb. ID; 1BNA), and different enzymes like MurD (pdb ID; 5A5E), MurF (pdb. ID; 4QDI), KdsB (pdb. ID; 3K8D) , KdsC (pdb. ID; 3HYC) and FabH (pdb. ID; 5A5E) crystal structures were reclaimed from protein data bank **[22]** and then immediately subjected to structure preparation and energy minimization in UCSF Chimera 1.15 **[23]**. In the phase of structure preparation, all coordinated ligand molecules expect necessary water molecules and ions are required for functionality of the biological picking out. In the energy minimization process, steepest descent and conjugate gradient algorithms were applied for each 1000 steps. To the biological picking out, 'Gasteiger charges' and hydrogen atoms were added in Auto-Dock 4.2.6 **[24]**. For docking with DNA molecule, the grid box was set 60 × 60 × 60 Å along the XYZ axis to cover entire DNA molecule for blind docking of the complex. In case of MurD, MurF, KdsB, KdsC and FabH, the grid box was maximized to cover the active pocket of enzymes. For the Zinc compound, at least 100

interactions were run and the one with best binding energy value (more negative) was selected and complexed with receptors. The docked complex was then visualized for docked conformation and interactions in UCSF Chimera 1.15 and Discovery Studio v2021 **[25]**.

2.6. Molecular Dynamics Simulation

Molecular dynamics simulation of the complex with minimum binding free energy was performed using AMBER 20 software **[26].** Antechamber was used to preprocess the complex **[27]**; the ff 14 SB was employed for protein molecule while GAFF force field **[28]** was used for the drug molecule. Minimization of the system was performed using a two-stage approach; the first the receptor molecule was kept fixed and minimized water and ions, followed by the entire system minimization. In the first phase, 1000 steps of minimization were conducted (500 steepest descent and 500 steps of the conjugate gradient) using constant volume periodic boundaries. In the process, a force constant of 500 kcal mol^{-1} angstrom was applied to restrain the receptor molecules and allowed free moves of the water molecules and counter ions. During the entire system minimization, 2500 steps were applied to the whole system without any restraints. the system was then heated up to 300 K using weak restraint on the NMR restraints overtime of 20 ps. AMBER uses Langevin temperature equilibration scheme (NTT=3) to maintain better and equalize the system temperature. SHAKE algorithm **[29]** was turn on to constrain bonds involving hydrogen atom, whereas Langevin dynamics **[30]** were occurred to control the temperature, keeping the collision frequency at 1.0 ps^{-1}. Then, the system was switched to constant pressure so that water density can relax and, at the same time to remove restraint on receptor by achieving temperature hold at 300 K. The equilibration was run for 100 ps to allow for systems enough time to relax. The equilibrium phase continues up to 50000 molecular dynamics steps with a time of 2 fs per step. The quality of the simulated systems was monitor by estimating each property for the system. This include root mean square deviation (RMSD) and root mean square fluctuation (RMSF)

using CPPTRAJ module **[31]** of AMBER. Further, MMPB\GBSA analysis was carried out using MMPBSA.py module to estimate binding free energies of the system **[32,33].**

2.7. Computational Details

- ***Hirshfeld Surface Analysis:***

To visualize and quantify the intermolecular contacts types and their impact on crystal packing in the environment of the crystal, Hirshfeld Surface Analysis have performed which is used to define the occupied space by molecule and partitioning electron density of the crystal into molecular fragments **[34].** The Crystal Explorer 17.5 software was used to calculate the Hirshfeld surface and their respective fingerprint plots for the Zn metal complex using Crystallographic Information File (CIF). The d_{norm} plot clearly shows the distances from outside nuclei surface (d_e) and inside surface (d_i), the color gradations for d_{norm} plot were fixed for the metal complex such as -0.83– 1.35 Å. The mapped color range for shaped index plot is -1.0 au − 1.0 au. In the d_{norm} surface, the sum of vdw radii shows in white surface, the short contact distances than vdw radii displays in blue surface and the close-contact interactions (hydrogen bond contacts) was shown in red surface on the three-dimensional (3D) Hirshfeld surfaces. In the shaped index, the blue and red color reflects the cycle stacking (the C−H···π and the π···π interactions). Moreover, the 2D fingerprint plots used to determine the contact distances to Hirshfeld Surface Analysis (di, de) which have shown the range from 0.6 to 2.8 Å including reciprocal contacts. In which, the different type of intermolecular interactions of the molecule in the crystal can be characterized by the shape of fingerprint plot.

- ***Density functional Theory***

The novel synthesized metal organic compound was optimized by B3LYP (DFT) with 6-311G* basis set **[35, 36,37, 38].** The atomic charges, HOMO, LUMO and electrostatic

potential map of the have analyzed from Gaussian09 **[38],** Gauss view **[39]** and 3D plot **[40]** software packages.

3. Results and discussion

3.1. Crystallographic description: Description of the crystal structure of $(C_{11}H_{18}N_2O)[Zn(SCN)_4]$

Single-crystal X-ray experiments revealed that the title complex crystallizes in the orthorhombic space group $P2_12_12_1$ with one tetra(isothiocyanate) $[Zn(SCN)_4]^{2-}$ anion and one $(C_{11}H_{18}N_2O)^{2+}$ cation in the unit cell. In fact, both **Fig 1** and **Fig 2** depict the asymmetric unit and the projection along the a-axis respectively. **Table S1 and S2** sum up the selected bond lengths and angles. The Zn is fourfold coordinated to four N-bonding thiocyanate anions and connected to one 1-(2- methoxyphenyl) piperazinium ligand using N—H ... S hydrogen bonds to build a three-dimensional network. For the tetra(isothiocyanate) $[Zn(NCS)_4]^{2-}$ anions, the coordination geometry of the central Zn (II) ions can be described as a slightly distorted tetrahedron. The average Zn -N bond distance is 1.939(4) A˚ and the N–Zn–N bond angles vary in the range 105.10(17)–113.89(17) ° for the anion containing the Zn1 atom. These values are in agreement with those found in complexes containing the tetra(isothiocyanate) $[Zn(NCS)_4]^{2-}$ anion, as seen in the structure of $(C_6H_7N)_2$ $Zn(SCN)_2$ **[41]**.

Fig 3 shows that the tetra(isothiocyanate) $[Zn(NCS)_4]^{2-}$ anions are arranged in pairs along the c-axis direction at (0, 0, 0), (½, 0, ½) and (½, ½, ½) to form anionic layers parallel to the (a,c) plane. The bond lengths around the central Zn atoms are comparable to those reported in literature **[41].** Besides, the bonding angles show that the tetraedron are slightly distorted; the Zn—N bond lengths are: (Zn1—N4=1.939(4) Å, Zn1—N3=1.944(4) Å, Zn1—N6=1.971(4) Å, Zn1—N5 =1.988(4) Å).

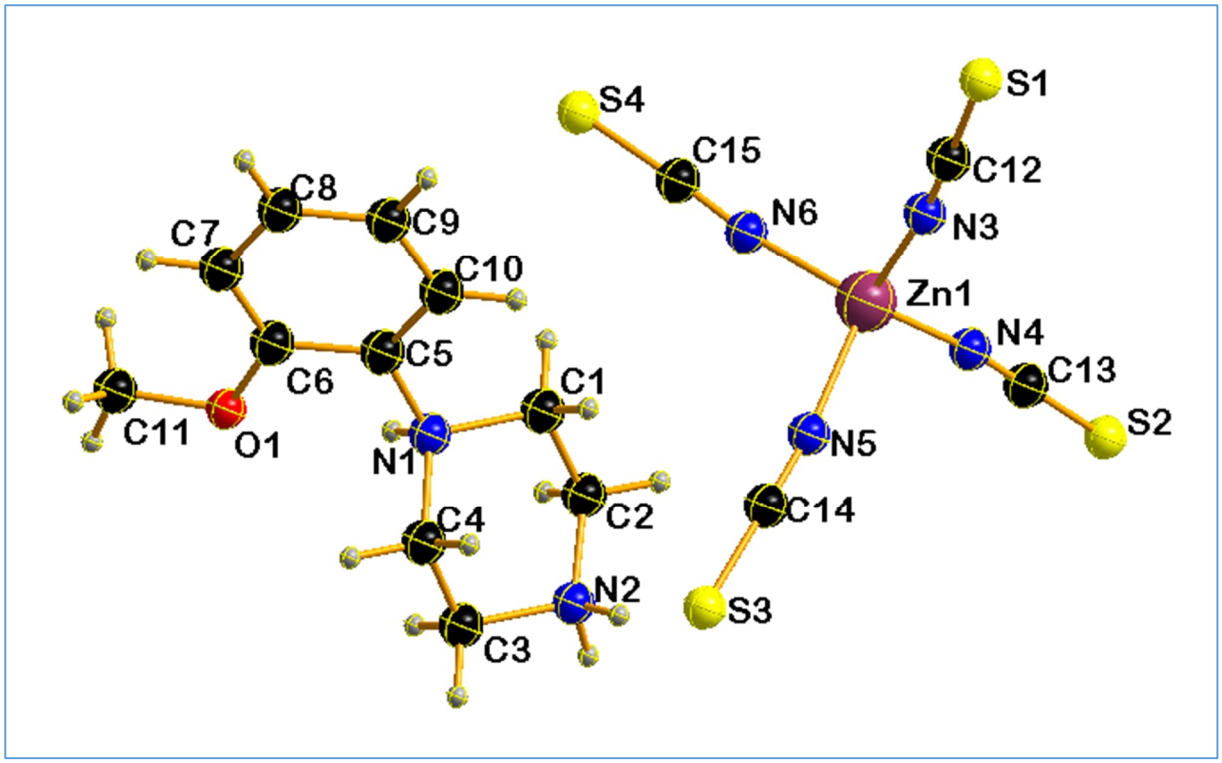

Figure 1: The asymmetric unit with atoms labeling for the compound

Table 2: hydrogen-bond geometry

Atoms D_H…A	Distance D…H [Å]	Distance H…A [Å]	Distance D…A [Å]	Angle D,H,A [°]
N1—H1...S1	0.92(2)	2.44(3)	3.326 (4)	162 (4)
N2—H2C…S2^{i}	0.91(2)	2.83(4)	3.405 (5)	123 (4)
N2—H2C…S3^{ii}	0.91(2)	2.64(3)	3.426 (4)	145 (4)
N2—H2D···S3^{iii}	0.91 (2)	2.39 (3)	3.274 (4)	163 (4)

Symmetry codes : (i) −x+1, y+1/2, −z+3/2 ; (ii) x−1/2, −y+3/2, −z+1 ; (iii) −x+1/2, −y+1, z+1/2.

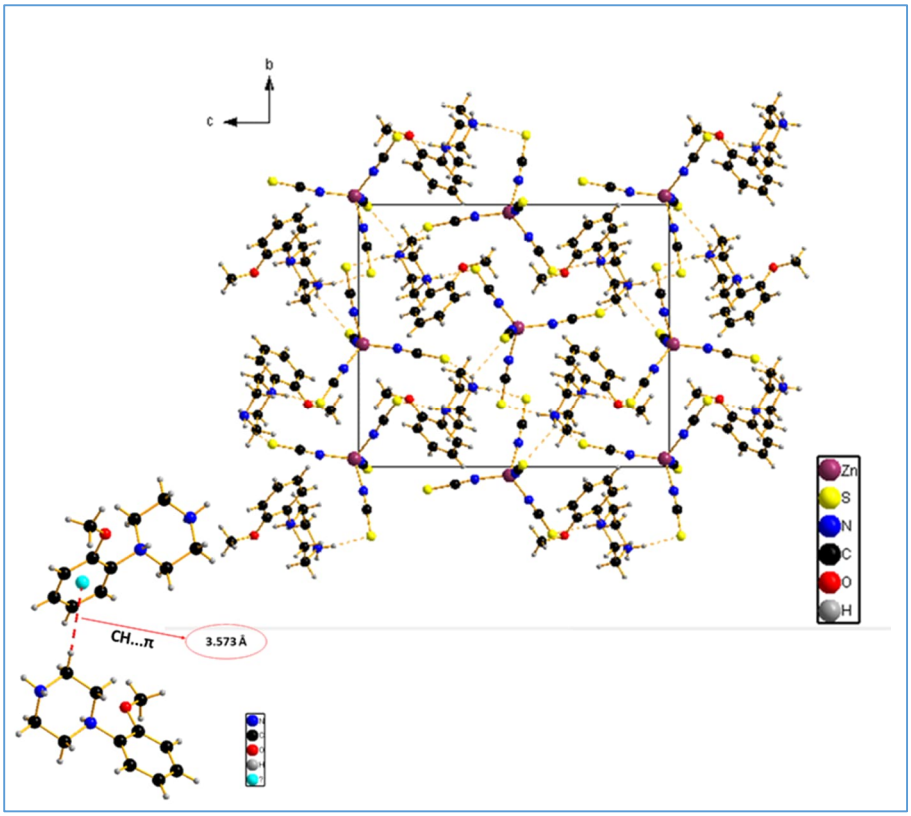

Figure 2 : Projection along the a-axis of the complex

Consequently, hydrogen-bonding interactions play a major role in the stability of the compound. The different types of H-bonds are shown in **Fig. 2** whereas; dashed light blue lines and their relative geometrical parameters are listed in **Table 2**. As a hydrogen donor, the organic molecule exhibits the N—H … S H-bond type which give rise to 3D chains of tetra(isothiocyanate) [Zn (NCS)$_4$]. On the other hand, the organic cation with its NH^+ groups display the N—H…S H-bond types which contribute to the linkage between the $[Zn(NCS)_4]^{2-}$ anions and the $(C_{11}H_{18}N_2O)^{2+}$ cations. All these intermolecular hydrogen bonds give rise to a three-dimensional network in the structure and contribute to the cohesion and stability of the compound. Regarding the donor-acceptor bond lengths, all the hydrogen bonds in the studied system are found to be weak (D—A > 3 Å) and have an electrostatic interaction type **[42].** It is noted that this topology of the thiocyanate network is usually observed for the based M(II) cations **[8].** C−H···π interactions plays the major role in the

crystal environment. Therefore, the corresponding value 3.573 Å, proves the stability of the coordination compound. The molecules establish intermolecular hydrogen-bonding interactions linking neighboring thiocyanate anions through N-H…S hydrogen bonds with lengths ranging respectively from 2.39 Å to 2.83 Å contributing to the $R\,\frac{1}{6}(36)$ ring as shown in **Fig. 4**.

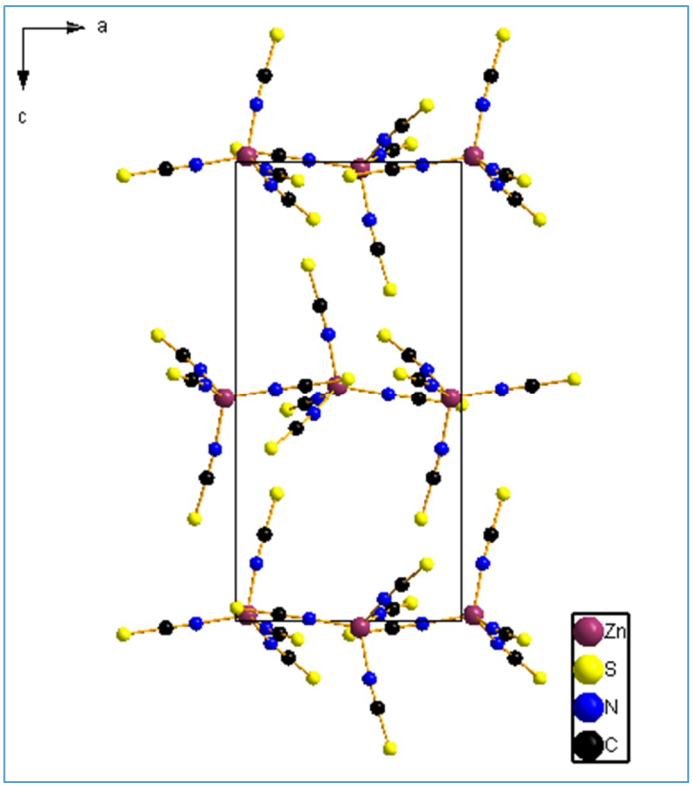

Figure 3: Projection along the a-axis of the anionic entity of the titled complex

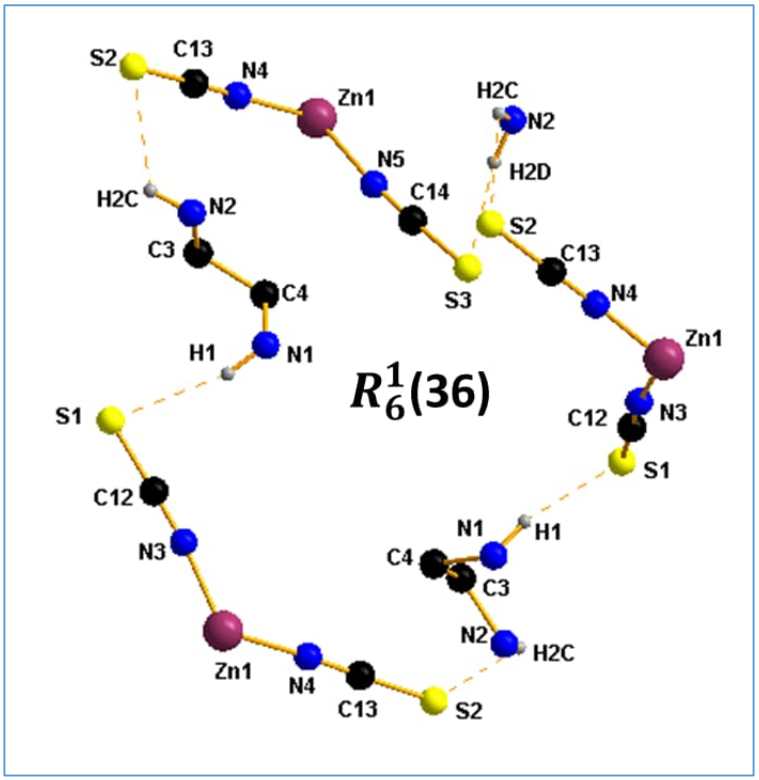

Figure 4: Intermolecular hydrogen bond ring of $(C_{11}H_{18}N_2O)$ $[Zn(SCN)_4]$

3.2. Experimental FT-IR studies of $(C_{11}H_{18}N_2O)[Zn(SCN)_4]$

Figure 5 shows the experimental infrared spectrum of the studied compound which is performed in KBr pellets**.** The prediction of the main FT-IR vibration frequencies of the $(C_{11}H_{18}N_2O)[Zn(SCN)_4]$ was carried out which represents the best obtained configuration.

The strong band at 2079 cm^{-1} can be assigned to the stretching vibration of the carbon-nitrogen triple bond of thiocyanic ligand. This vibration assignments of thiocyanate indicates the binding of thiocyanate ligand to Metal (II) center via its N-terminal atom. The assignment of these bands to thiocyanate vibrations and the determination of its coordination mode are based on previously reported results such as for $(C_2N_6H_{12})[Co(NCS)_4]$. H_2O **[44]**, and $2(C_5H_7N_2)[Ni(SCN)_4]$ **[45].**

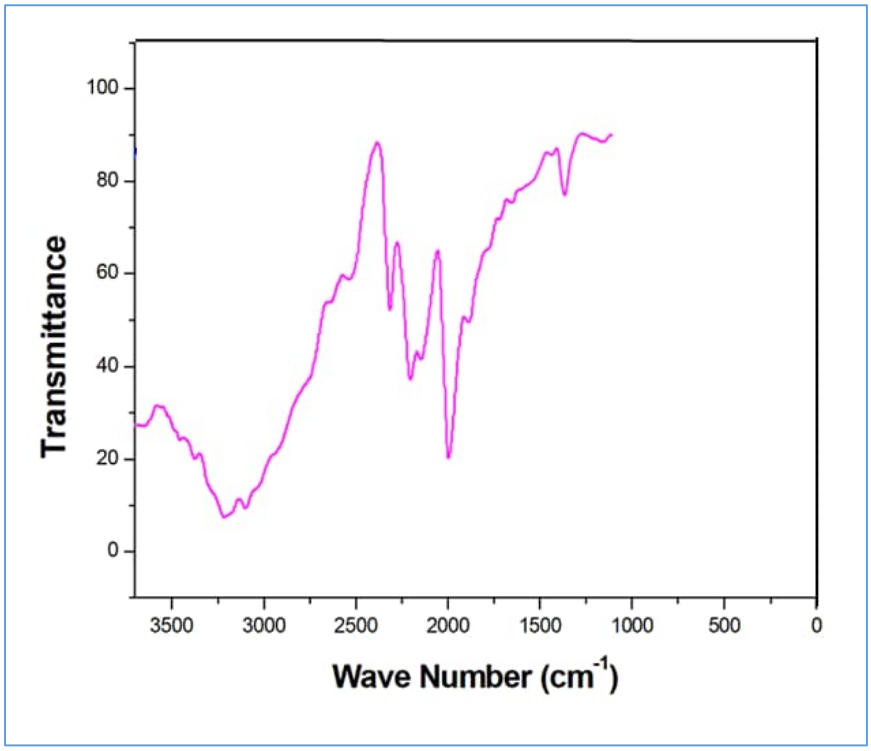

Figure 5: Experimental FTIR spectrum of ($C_{11}H_{18}N_2O$) [$Zn(SCN)_4$]

The spectrum shows also characteristic vibrations for organic cations. The broad bands in the range 3600 - 2300 cm^{-1} correspond to the stretching vibrations of the organic and hydroxyl groups ν(N–H) and ν(C–H). The band at 1504 cm^{-1} corresponds to ν(C = C) stretching vibrations. The band at 1450 cm^{-1} can be assigned to the CH_2 deformation. The frequency observed at 3128 cm^{-1} in the FT-IR experimental spectra is assigned as the C-H stretching modes of the phenyl rings **[46].** The bands at 1244 and 1180 cm^{-1} can be attributed to the ring deformation. The weak bands at 1166 and 1021 cm^{-1} can be assigned to the CH_2 twisting **[47].**

3.3. Solid and liquid state UV–vis spectrum analysis

The optical properties of our compound have been studied in solution in dimethyl sulfoxide (DMSO) (10^{-2} mol. L^{-1}) as a solvent for the liquid state analysis. **Figure 6** highlights for ($C_{11}H_{18}N_2O$) [Zn (SCN)$_4$] the presence of a wide band at 410 nm which can be attributed to the transitions (π-π*) of the aromatic cycle of 1- (2-methoxyphenyl) piperazine adding a band

located at 505 nm and the band located at 650 nm corresponds to group type transitions (n -π*) of the (C≡S) at the solid-state spectrum. Furthermore, these results are confirmed by the liquid state spectrum which gibes a band at 500 nm attributed to the transitions (π-π*) of the aromatic cycle and a band at 580 nm corresponds to group type transitions (n -π*) of the (C≡S).

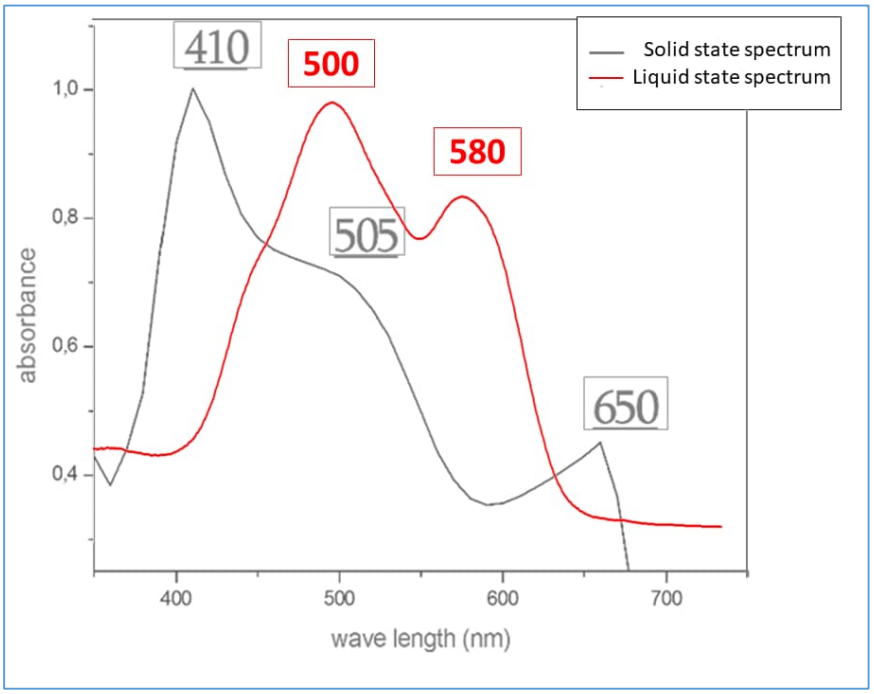

Figure 6: UV–vis spectrum analysis of $(C_{11}H_{18}N_2O)$ $[Zn(SCN)_4]$

3.4. Thermal analyses (thermogravimetric and differential thermal analysis)

In order to follow the thermal behavior of title compound, we undertook a thermal study by differential thermal analysis (DTA) and thermogravimetric (TGA). The measurements were carried out at a temperature interval between 273 and 573 K on a sample of 9.39 mg for $(C_{11}H_{18}N_2O)[Zn(SCN)_4]$ and a heating rate of 5 °. min^{-1} using a multimodule 92 Stream device. In this context it was checked if a different, metastable modification of $(C_{11}H_{18}N_2O)[Zn(SCN)_4]$ can be obtained as recently reported for other ligands **[48-50].**

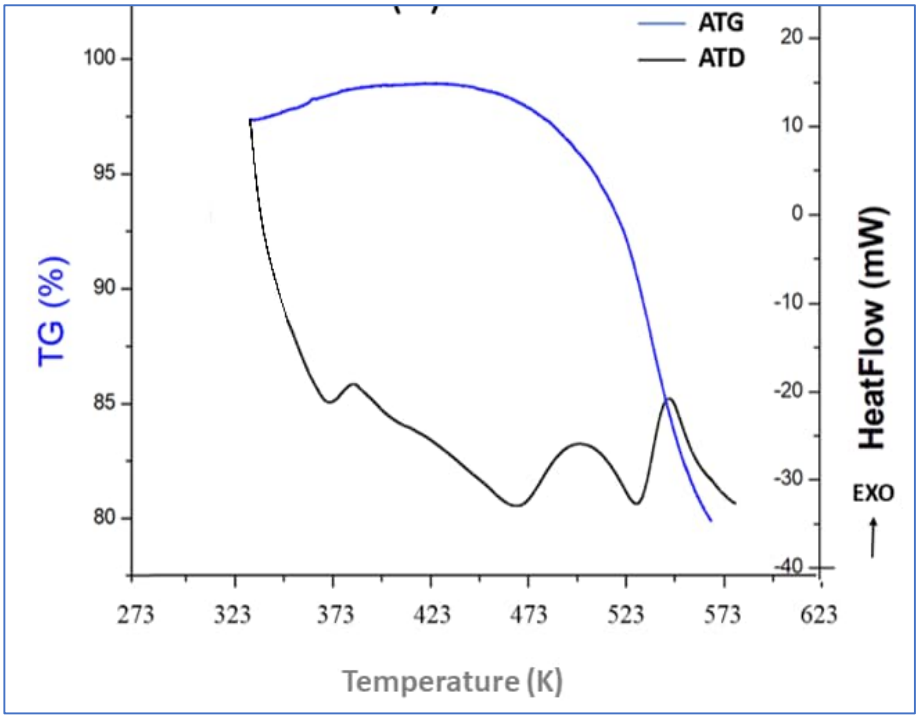

Figure 7: The DTA / GTA thermogram of ($C_{11}H_{18}N_2O$) $[Zn(SCN)_4]$

The DTA thermogram (**Figure 7**) shows for ($C_{11}H_{18}N_2O$)$[Zn(SCN)_4]$ weight losses in the [323, 523 K] range, complying with the decomposition of the organic part, and some of the thiocyanate ligands from the metal. At a high temperature, the decomposition of the compound give rise to gaseous evolution of thiocyanic acid contaminated with carbon black which is in particular toxic gas. The decomposition in the [500–547 K] range has the same variation for the two compounds, it's the decomposition of the resulting $M(NCS)_4$ and $M(NCS)_2$ is carried out at a higher temperature **[51].**

3.5. Antibacterial activity

First, the diffusion agar technique was used to evaluate the antibacterial activity of synthesized compound, the inhibition zone diameters were measured (shown in **Table 3** and schematically presented in **Figure 8**). Hence, the compound clearly presented positive results against the tested bacteria.

Table 3: Diameters of measured zones of inhibition of ($C_{11}H_{18}N_2O$) [$Zn(SCN)_4$] against bacteria tested.

	Inhibition diameter (mm)				
	Ampicilline/ Nystatine	**Extract**			
Disc load (µg) / **Bacterial strain name**	**10µg/100µg**	**($C_{11}H_{18}N_2O$) [Zn (SCN)$_4$]** **0.50mg**	**1mg**	**1.50 mg**	**2mg**
Salmonella typhimurium ATCC 14028 G(-)	14.75±1.0	11.05±0.1	11.75±0.3	12.5±0.6	**15.01±0.4**
Staphylococcus aureus ATCC 6538 G(+)	17.5±0.7	10.00±0.3	11.75±1.0	11.83±0.2	**13.0±0.3**
Candida albicans ATCC 10231	16.83±0.2	9.20±0.0	10.5±0.7	11.02±0.7	**12.5±0.7**

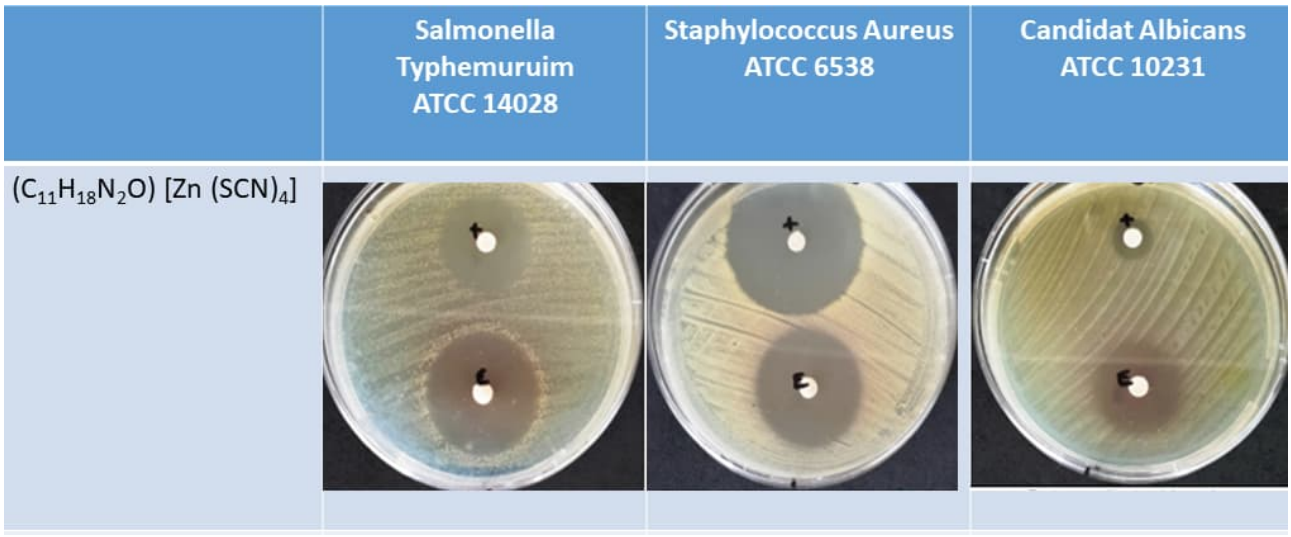

Figure 8: The inhibition zone diameters.

Accordingly, the antibacterial activity of ($C_{11}H_{18}N_2O$) [$Zn(SCN)_4$] was evaluated against gram-negative pathogenic strains: *Salmonella typhimurium* **[52]** ATCC 14028 G (-), as well as with gram-positive: *Staphylococcus aureus* ATCC 6538 G (+), It was also tested by *Candida albicans* **[53]** ATCC 10231.

The antibacterial activity of ($C_{11}H_{18}N_2O$) [$Zn (SCN)_4$] was tested against three bacterial strains for different extracts of 0.50, 1, 1.50 and 2 mg. As illustrated in **Table 3**, the findings

of the microbial activities of ($C_{11}H_{18}N_2O$) [Zn (SCN) $_4$]. The examination of these results has proved that the synthesized compound manifested an effective antibacterial power against the gram-negative bacteria *Salmonella typhimurium* ATCC 14028 G (-). This good activity has been demonstrated with a diameter inhibition zone of 15.01 ± 0.4 at a concentration of 2 mg. This bacterium has an inhibition diameter of value 14,75±1.0, which prove the great efficiency of ($C_{11}H_{18}N_2O$) [Zn(SCN) $_4$]. The inhibition action happens mainly due to the synergy between the cation in which the functionalization of the methoxy phenyl unit leads to promising antibacterial activities against the selected pathogenic strains which indicate the importance of the cationic group in the crystal structure of this compound and the anionic part [$Zn(SCN)_4$] which gives rise to a network of hydrogen bonds that destroys the multiplication process.

3.6. Molecular Docking

Molecular docking is a powerful technique to find binding of compounds with biological macromolecule and allows the identification of correct intermolecular binding conformation **[54].** The docking binding energy of the compounds with various antibacterial targets is illustrated in **Table 4**. The complex revealed good binding energy with all targets in particular the compound shows an excellent binding energy with MurF enzyme. This enzyme is involved in bacterial cell wall biosynthesis and is localized the cytoplasm. The enzyme is thought to be a key antibacterial target due to its selective and specific nature in bacterial survival **[55]**. In case of zinc compound, the molecule favor docking at the same ATP side as that seen for copper compound. The compound is engaged by multiple interactions from several residues of the ATP binding side **(Figure 9)**. The compound shows chemical interactions with Ser123, Lys125, Thr126, Thr127, Asn206, His292, Asn293, Arg327, Leu328, Tyr343, Asn344, Ala345, Thr348, and Ser34.

Table 4: Autodock binding free energy of the compounds with different antibacterial targets.

Complex	Biological Targets					
	DNA	**MurF**	**MurD**	**KdsB**	**KdsC**	**FabH**
Zinc Complex	-8.35	-13.89	-12.34	-10.00	-8.01	-10.58

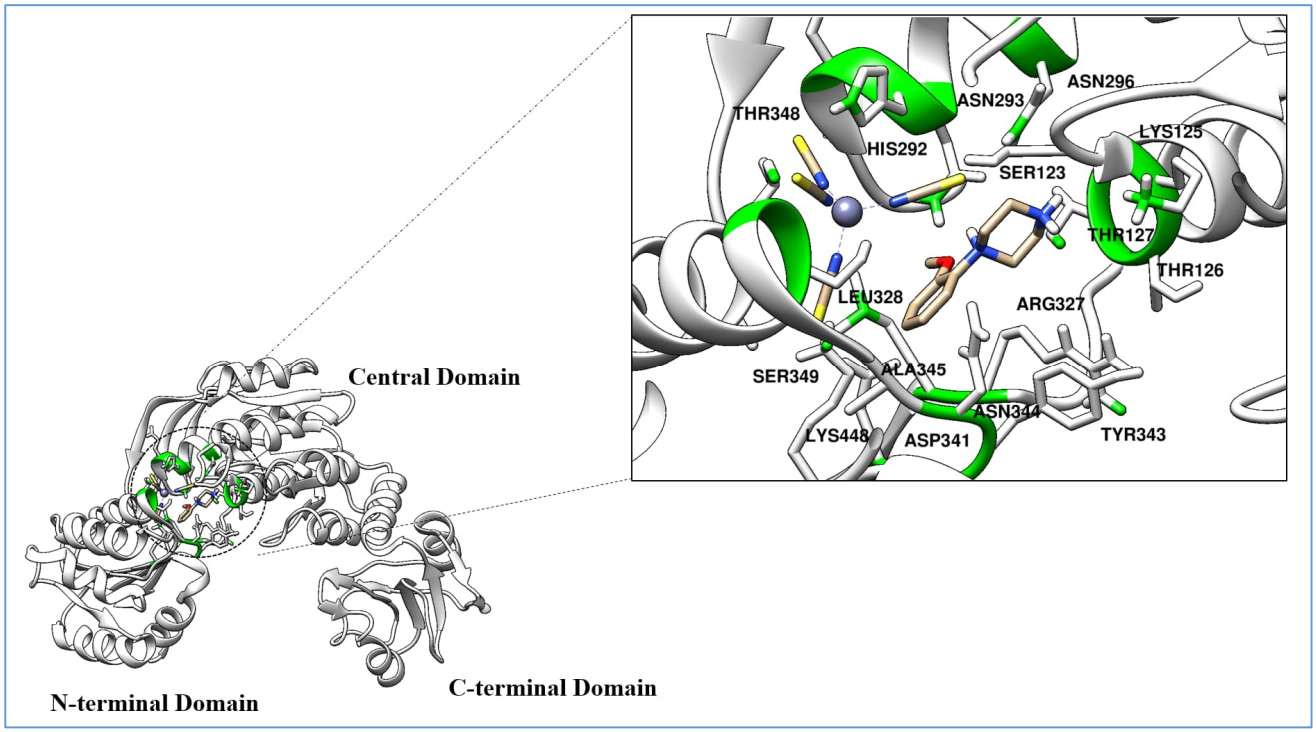

Figure 9: Binding conformation and interactions of zinc compound at ATP binding site of MurF. The MurF is shown by white cartoon, the compound is shown by tan stick, while green color represents within 3 Å interacting residues

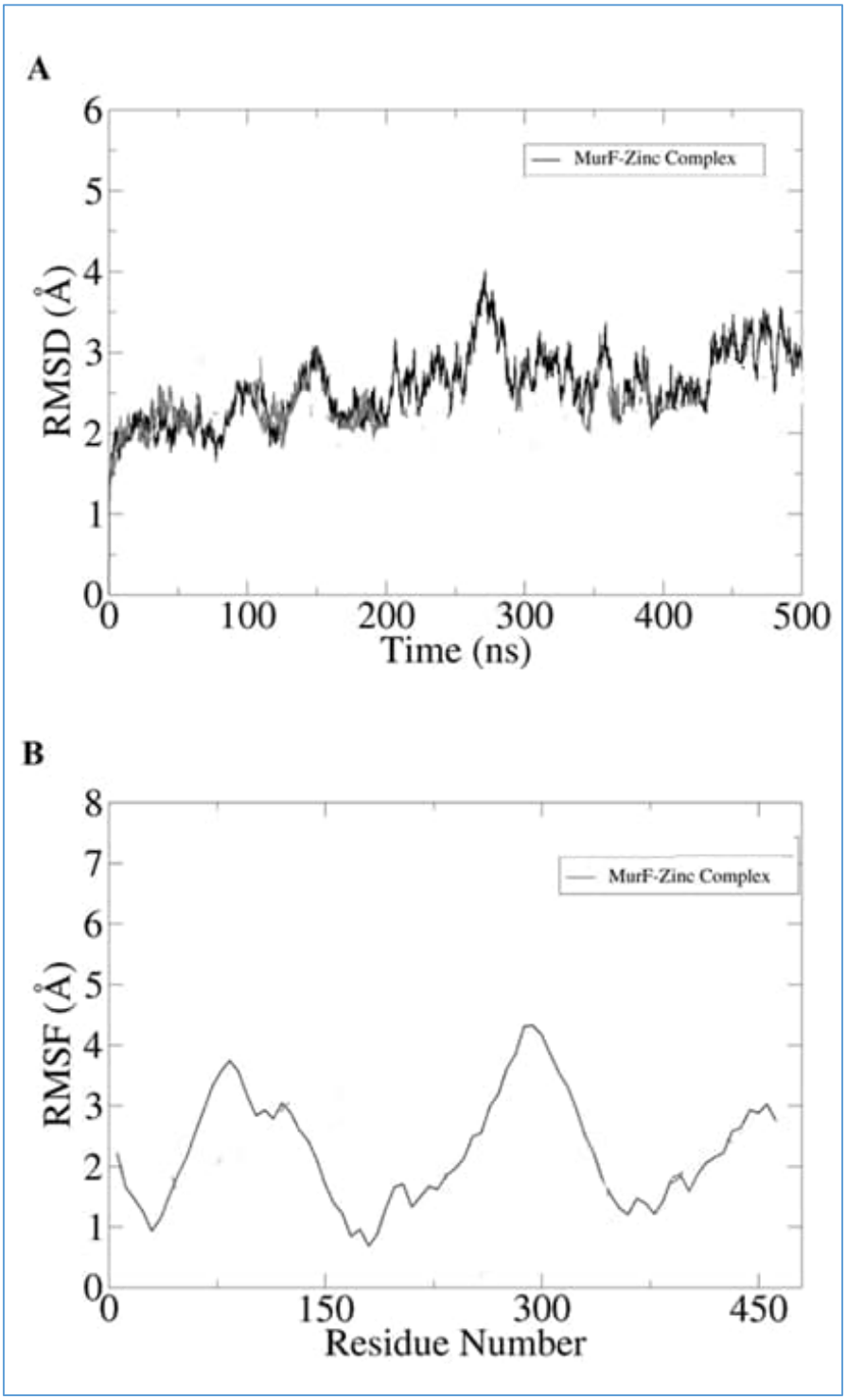

Figure 10: Evaluation of structure stability of MurF in the presence of compounds. **A.** RMSD and **B.** RMSF.

3.7. Molecular Dynamics Simulation

The docked complex was subjected to molecular dynamics simulation to decipher it dynamics and stability of intermolecular binding. The complex stability was evaluated using root mean square deviation (RMSD) **[56]** and residues based root mean square fluctuation (RMSF) **[57]**. According to RMSD, the MurF-zinc complex is stable (**figure 10**). The former has some fluctuation in the initial 100 ns, followed by stable structure behavior in the rest of simulation time. The RMSD for this complex fluctuates ~ 2 Å. MurF-zinc complex though remain within acceptable RMSD deviations, but minor fluctuations (> 3 Å) in between 200-300 ns, and in the last 50 ns were noticed. This deviation though upon visualization of the simulation trajectories does not affect the binding of the compound at the active pocket.

In RMSD, the residues can be seen in consistent fluctuations in the presence of the compound, but still these changes have no impact on the compound binding conformation at the docked site. Interestingly, the active pocket residues (Ser123, Lys125, Thr126, Thr127, Asn206, His292, Asn293, Arg327, Leu328, Tyr343, Asn344, Ala345, Thr348, and Ser34) were noticed in good stability (RMSF value < 3 Å) in the compound's presence.

3.8. MMPB\GBSA Analysis

Binding free energy methods are useful in predicting different interactions energies between drug and its receptor molecule. These methods are less computationally less expensive, moderately accurate and are comparable to experimental findings. The Zn complex reveals stable docked conformation energies with the MurF receptor. Furthermore, the van der Waals energy was found to dominate other energies in term of its contribution in docked intermolecular conformation. The electrostatic energy also seems to play a key role in make the complex stable. Because of good contribution from van der Waal as well as from electrostatic energies, the net gas phase energy is favorable. The polar solvation energy in contrast was disclosed to be least favorable in complex formation than the non-polar

solvation energy. The zinc complex on the other hand, has net binding energy of -25.53 kcal.mol^{-1} and -22.89 kcal.mol^{-1} in MM-GBSA and MM-PBSA, respectively. Details of MMPB\GBSA are illustrated in **Table 5**.

Table 5: Estimated binding free energies for simulated complex. Each value is given in kcal.mol.

Energy Parameter	Zinc Complex
MM-GBSA	
Van der Waals Energy	-30.28
Electrostatic Energy	-14.97
Gas Phase Energy	-45.25
Solvation Energy	19.72
Net Energy	-25.53
MM-PBSA	
Van der Waals Energy	-30.28
Electrostatic Energy	-14.97
Gas Phase Energy	-45.25
Solvation Energy	22.36
Net Energy	-22.89

3.9. Hirshfeld surface calculations

The d_{norm} and shape index plot of the complex was shown in **Figure 11.** In which, blue and white surfaces are higher than red surfaces in the complex due to hydrophobic areas**.** There are some dark red regions are appeared around the metal bonding region in the complex such as N–H…S and C–H…S type of interactions in the Zn complex. However, the intensity and the sizes of these red spots are not the same around the Sulfur and nitrogen atoms due to the distance between the atoms involved in the short contact is directly proportional to the intensity and the size of the red spots in the d_{norm} map. Whereas, the dark red and blue surfaces of the shaped index indicate the C−H…π interactions in the crystal. Fingerprint plots are used to quantify the contribution of different type of interactions in the solid state (**Figure11).** The corresponding fingerprint plot of the complex is shown with characteristic pseudo-symmetric wings in the d_e and d_i diagonal axes which are delineated into

Zn…S/S…Zn, C...H/H...C, S...H/H...S, N...H/H...N, H...H contacts in the complex. The contribution of H···H, N···H and S···H type of interactions are highly presented in the Zn complex which also confirms that the vdw and C–H···π interactions plays the major role in the crystal environment. Therefore, this fingerprint plot clearly confirms weak hydrogen bonding that shows the stability of the coordination compound.

3.10. Frontier molecular orbital analysis

Highest occupied molecular orbital (HOMO) and lowest unoccupied molecular orbital (LUMO) of quantum chemical descriptors were calculated for the metal organic complex; it's highly related to chemical and biological activities. The molecular surface of HOMO and LUMO maps of the compound was drawn at 0.2 au and shown in **Figure 12**; in which, the HOMO and LUMO energy surface in Zn complex, it was found around the S and other atoms in the molecule but not over Zn atom. The blue and red colors indicate positive and negative regions.

The charge injection and transporting properties of metal coordination molecule is an important which was calculated from the global reactivity descriptors. The HOMO and LUMO energies are responsible for the charge transfer in a chemical reaction **[58].** All the calculated global reactivity descriptors (such as electronegativity, global hardness, electrophilicity and HOMO-LUMO energies) are tabulated (**Table S3)**. In which, the band gap of the Zn complex is low, however, this low band gap energies confirmed high chemical reactivity, optical polarizability and low kinetic stability.

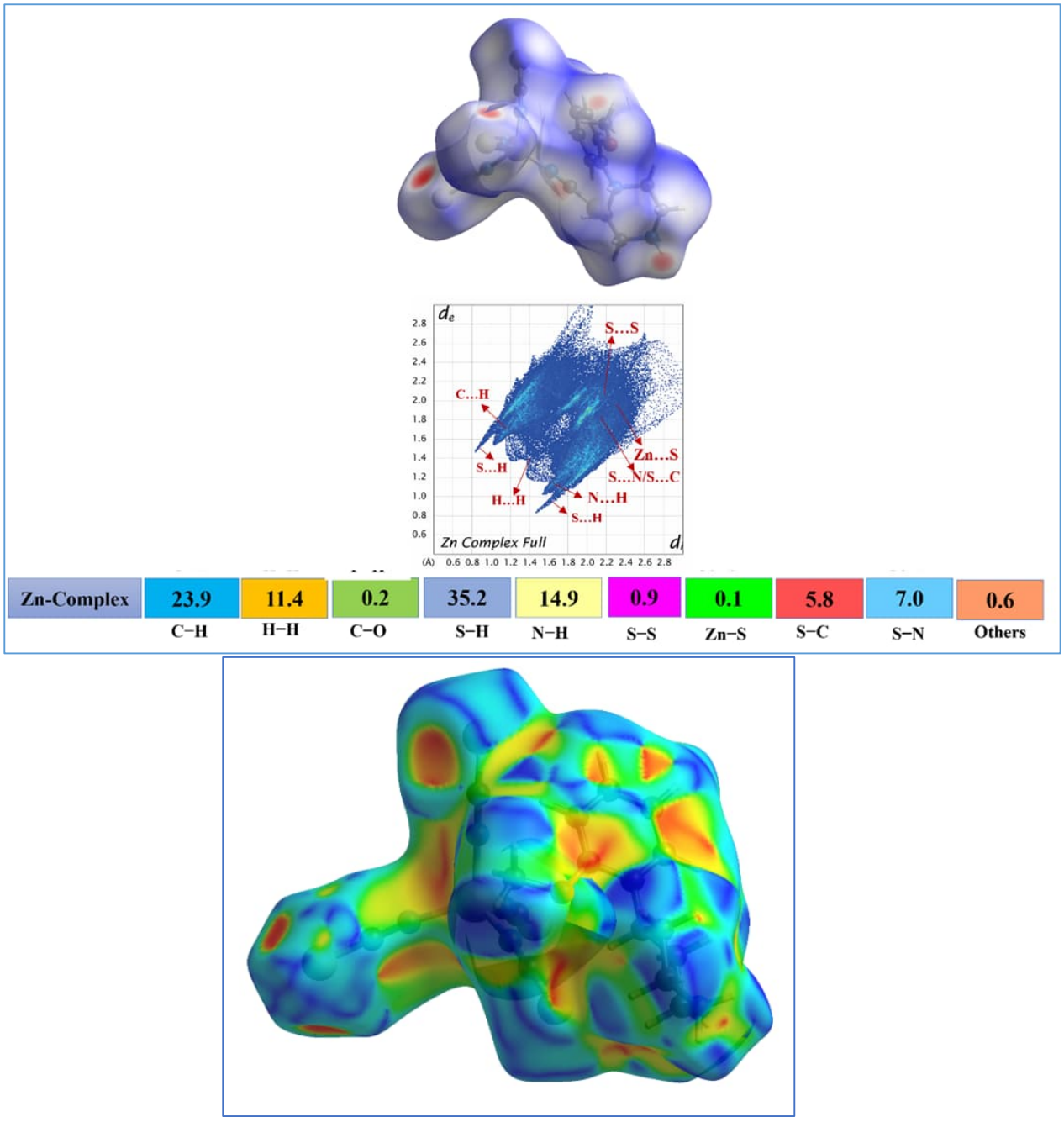

Figure 11: Hirshfeld Surface Analysis mapped with d_{norm}, Fingerprint plots and shaped index for the Zn complex

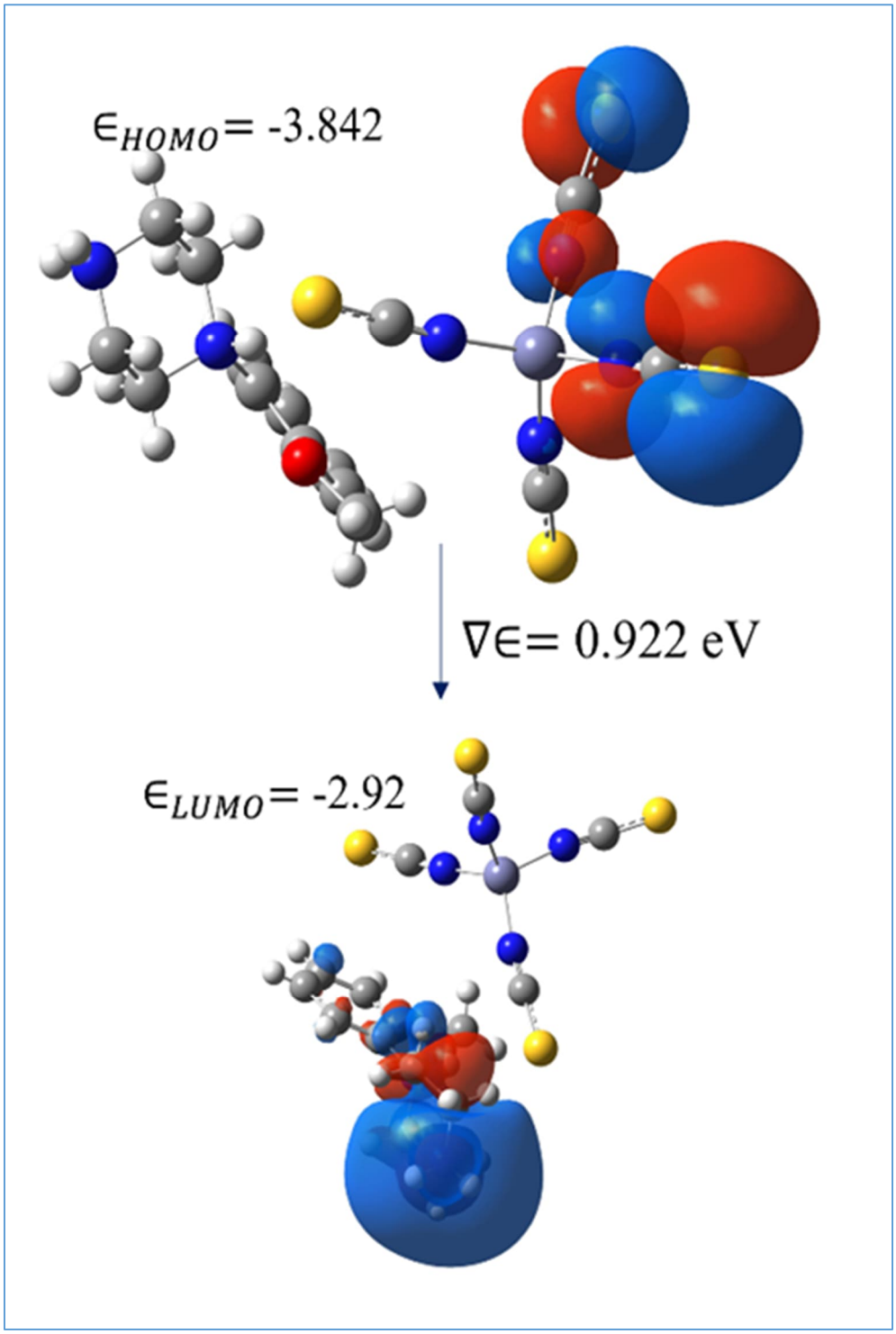

Figure 12: HOMO and LUMO of the Zn-Complex.

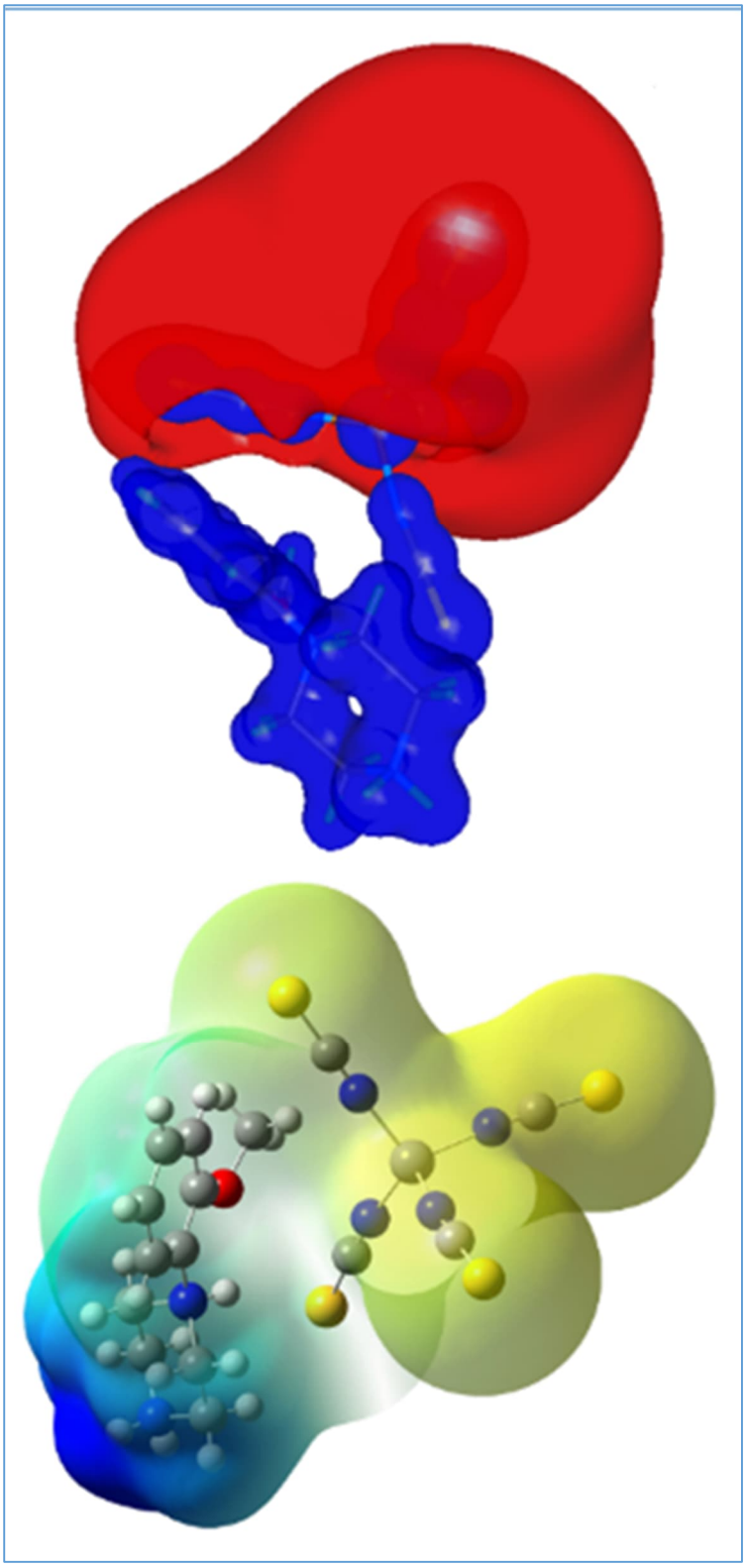

Figure 13: Isosurface representation of the molecular electrostatic potential of two metal compounds. Blue: positive potential, Red: negative potential. The surface values are +0.7 and -0.07eÅ^{-1} of the Zn-Complex.

3.11. Electrostatic potential map

Electrostatic potential map helps to predict the possible reactive sites of the molecule where the nucleophilic (attracted to regions with positive potential) and electrophilic (attracted towards the regions with negative potential) regions present in the molecule. **Figure 13** shows the iso-surface representation of the molecular electrostatic potential (MSP) of the metal compound. The large electronegative regions (red surface) are found over the sulfur atom region and the blue surface acts as an electrophilic site. This large negative electrostatic potential of S atom can participate in forming of S–H interactions.

3.12. Nonlinear optical properties (NLO)

In recent years, the NLO materials got huge interest thanks to their broad-range of applications like signal processing, optoelectronic technologies, optical switching and data storage **[59].** Therefore, the novel NLO materials exhibit different technological applications that leads their importance. Further, metal-based organometallic complexes exhibit outstanding electrochemical and optical properties than the organic and inorganic compounds. In this regard, here, we studied the NLO properties of a Zn metal complex using quantum chemical calculation, performed at B3LYP/LANL2DZ level of basis set in gaussian 09 software package**.** The total dipole moment (μ), the average and anisotropy of polarizability (α & Δα) and hyperpolarizabilities (β) were calculated using following equations (1-4).

$$\mu = \sqrt{\mu_x^2 + \mu_y^2 + \mu_z^2} \quad (1)$$

$$\alpha = \frac{1}{3}(\alpha_{xx} + \alpha_{yy} + \alpha_{zz}) \quad (2)$$

$$\Delta\alpha = \sqrt{\frac{1}{2}[(\alpha_{xx} - \alpha_{yy})^2 + (\alpha_{yy} - \alpha_{zz})^2 + (\alpha_{zz} - \alpha_{xx})^2 + 6\alpha_{xz}^2]} \quad (3)$$

$$\beta = \sqrt{[(\beta_{xxx} + \beta_{xyy} + \beta_{xzz})^2 + (\beta_{yyy} + \beta_{yzz} + \beta_{yxx})^2 + (\beta_{zzz} + \beta_{zxx} + \beta_{zyy})^2]} \quad (4)$$

These values are calculated and converted from atomic units (a.u) to electrostatic units (esu) with the help of conversion factor (α: 0.1482 × 10^{-24} esu & β: 8.6393 × 10^{-33} esu). To evaluate these results (**Table S4**), NLO properties of KDP and urea were compared as reference. The computed dipole moment of Zn complex is higher than urea and lower than KDP**.** The hyperpolarizability parameter of the Zn-metal complex is higher ~24 times higher than the KDP and 89 times higher than the urea respectively. Therefore, this metal complex is an efficacious candidate for NLO materials.

3.13. Natural bond orbital analysis (NBO)

NBO calculations interests on the role of intermolecular orbital interaction in the complex structure, it is a self-consistent theoretical framework to characterize the nature of chemical bonding in molecules and materials. Particularly, it helps to study about charge transfer between donor (filled NBO's) and acceptor (empty NBO's). To estimate the stabilization energy, the following second-order perturbation theory is used.

$$E^{(2)} = q_i \frac{(F_{i,j})^2}{\varepsilon_j - \varepsilon_i}$$

In order to characterize the coordination bonds as well as to identify the contribution of interactions to stabilize the synthesized complex. Generally, the molecular interactions are formed by overlapping the orbitals between σ and σ*, resulting intermolecular charge transfer to stabilize the molecular system. Therefore, NBO analysis of the metal complex was performed by B3LYP/LanL2DZ level of DFT method**.** (**Table S5**) shows the selected donor and acceptor orbitals along with their description, hybridization of atoms, occupancy of the orbitals and stabilization energies. In the Zn complex, the stabilization energy of same kind of interaction Zn…N is 60.32 kcal.mol^{-1}. These higher stabilization energy of hyper conjugative

interaction carries higher energy which leads to elongate their corresponding bonds. Notably, due to the charge transfer character of metal-organic complex, the stabilization energy of *metal to ligand* is lower than the *ligand to metal* which enhances NLO activity of the molecules.

4. Conclusion

The synthesis and characterization of novel coordination compound *($C_{11}H_{18}N_2O$) [$Zn(SCN)_4$]*, has been described and optimized. In the Zinc-complex; the metal center was found to be tetracoordinated with four NCS entities establishing a tetrahedral geometry. The intermolecular cohesion is ensured by N–H…S hydrogen bonds and CH-π interactions. In addition, the optical properties were investigated by FT-IR absorption measurement add to liquid and solid state Ultra-violet measurements. A thermal study by differential thermal analysis (DTA) and thermal gravimetric analysis (TGA) which highlights the stability and the decomposition ranges. Hirshfeld surface analysis shows the main interactions responsible for molecular packing in complex structure. The HOMO-LUMO and quantum descriptors helps to study the charge transfer and chemical reactivity. The ESP map shows large electronegative regions (red surface) over the sulfur atom. A high NLO properties of Zn-metal complex is obtained and the high stabilization energy from metal to ligand confirmed the NLO activity. The antibacterial assay also proves a high efficiency against different tested bacteria. The antibacterial activity of the compounds was cross validated by molecular docking and simulation analysis that proved the binding potential of the compound for several antibacterial targets particularly the MurF enzyme. The enzyme revealed several key active site residues to form short distance hydrophilic and hydrophobic contacts with the compound. These results are a good indication that the nature of the metal used has an important effect on the coordination compounds characterization.

Appendix A. Supplementary material

A CCDC Deposition Number 2081694 contain the supplementary crystallographic data for the Zn complex. This data can be obtained free of charge via http://www.ccdc.cam.ac.uk/conts/retrieving.html, or from the Cambridge Crystallographic Data Center, 12 Union Road, Cambridge CB2 1EZ, UK; fax: (+44) 1223-336-033; or email: deposit@ccdc.cam.ac.uk.

References

[1] Y. P. Prananto, A. Urbatsch, B. Moubaraki, K. S. Murray, D. R.Turner, G. B. Deacon, S. R. Batten, Aust. J. Chem. 2017, 70, 516–528.

[2] D. A. Buckingham, Coord. Chem. Rev. 1994, 135, 587–621.

[3] S. S. Massoud, A. E. Guilbeau, H. T. Luong, R. Vicente, J. H.Albering, R. C. Fischer,F.A. Mautner, Polyhedron 2013, 54, 26–33.

[4] A. Jochim, M. Rams, T. Neumann, C. Wellm, H. Reinsch, G. M.Wójtowicz, C. Näther, Eur. J. Inorg. Chem. 2018, 2018, 4779–4789..

[5] J. Palion-Gazda, B. Machura, F. Lloret, M. Julve, Cryst. GrowthDes. 2015, 15, 2380–2388.

[6] C. D. Mekuimemba, F. Conan, A. J. Mota, M. A. Palacios, E. Colacio,S. Triki, Inorg. Chem. 2018, 57, 2184–2192.

[7] F. A. Mautner, M. Traber, R. C. Fischer, A. Torvisco, K.Reichmann, S. Speed, R. Vicente, S. S. Massoud, Polyhedron2018, 154, 436–442.

[8] T. Neumann, M. Ceglarska, M. Rams, L. S. Germann, R. E.Dinnebier, S. Suckert, I. Jess, C. Näther, Inorg. Chem. 2018, 57,3305–3314.

[9] S. Suckert, M. Rams, L. Germann, D. M. Cegiełka, R. E. Dinnebier,C. Näther, Cryst. Growth Des. 2017, 17, 3997–4005.

[10] K. Müller-Buschbaum, Z. Anorg. Allg. Chem. 2005, 631, 811–828.

[11] F. Schönfeld, L. V. Meyer, F. Winter, O. Niehaus, U. C. Rodewald,R. Pöttgen, K. Müller-Buschbaum, Z. Anorg. Allg. Chem.2012, 638, 2062–2068.

[12] C. J. Höller, K. Müller-Buschbaum, Inorg. Chem. 2008, 47,10141–10149

[13] M. Đaković, M. Došen, Z. Popović, Journal of chemical crystallography, 41 (2011) 180-185.

[14] S.C. Manna, A.D. Jana, M.G.B. Drew, G. Mostafa, N.R. Chaudhuri, Polyhedron, 27 (2008) 1280-1286.

[15] J. Boeckmann, B. Reimer, C. Nather, Journal of Chemical Sciences, 66 (2011) 819-827.

[16] P. Nithya, S. Helena, J. Simpson, M. Ilanchelian, A. Muthusankar, S. Govindarajan, Journal of Photochemistry and Photobiology B-Biology, 165 (2016) 220-231.

[17] S.J. Osborne, S. Wellens, C. Ward, S. Felton, R.M. Bowman, K. Binnemans, M. Swadźba-Kwaśny, H.N.Gunaratne, P. Nockemann, Dalton Transactions, 44 (2015) 11286-11289.

[18] G. Sheldrick, Acta Crystallogr. Sect. A 71, 3(2015).

[19] Farrugia LJ (1999) WinGX suite for small-molecule single-crystal crystallography. J Appl Crystallogr 32:837–838.

[20] K.R. Cousins, Computer review of ChemDraw ultra 12.0, (2011).

[21] T. a Halgren, Merck Molecular Force Field., J. Comput. Chem. 17 (1996) 490–519.

[22] J.L. Sussman, D. Lin, J. Jiang, N.O. Manning, J. Prilusky, O. Ritter, E.E. Abola, Acta Crystallogr. Sect. D Biol. Crystallogr. 54 (1998) 1078–1084.

[23] E.F. Pettersen, T.D. Goddard, C.C. Huang, G.S. Couch, D.M. Greenblatt, E.C. Meng, T.E. Ferrin, J. Comput. Chem. 25 (2004) 1605–1612.

[24] G.M. Morris, R. Huey, W. Lindstrom, M.F. Sanner, R.K. Belew, D.S. Goodsell, A.J. Olson, J. Comput. Chem. 30 (2009) 2785–2791.

[25] D.S. Biovia, Discovery studio visualizer, San Diego, CA, USA. (2017).

[26] D.A. Case, K. Belfon, I. Ben-Shalom, S.R. Brozell, D. Cerutti, T. Cheatham, V.W.D. Cruzeiro, T. Darden, R.E. Duke, G. Giambasu, others, Amber 2020, (2020).

[27] J. Wang, W. Wang, P.A. Kollman, D.A. J. Am. Chem. Soc. 222 (2001) U403.

[28] X. He, S. Liu, T.-S. Lee, B. Ji, V.H. Man, D.M. York, J. Wang, , ACS Omega. 5 (2020) 4611–4619.

[29] V. Kräutler, W.F. Van Gunsteren, P.H. Hünenberger, J. Comput. Chem. 22 (2001) 501–508.

[30] J.A. Izaguirre, D.P. Catarello, J.M. Wozniak, R.D. Skeel, J. Chem. Phys. 114 (2001) 2090–2098.

[31] D.R. Roe, T.E. Cheatham III, PTRAJ and CPPTRAJ, J. Chem. Theory Comput. 9 (2013) 3084–3095.

[32] B.R. Miller, T.D. McGee, J.M. Swails, N. Homeyer, H. Gohlke, A.E. Roitberg, J. Chem. Theory Comput. 8 (2012) 3314–3321.

[33] S. Genheden, U. Ryde, Drug Discov. 10 (2015) 449–461.

[34] Spackman, M. A., & Jayatilaka, D. CrystEngComm, (2009). 11, 19-32.

[35] Labanowski, J. K., & Andzelm, J. W. Springer. (1991).

[36] Parr, R. G., & Yang, W. Univ. Press, (1989).

[37] Davidson, R. E., & Feller, D. Chemical Reviews, (1988). 86, 661–696.

[38] Frisch, M. J., Trucks, G. W., Schlegel, H. B., Scuseria, G. E., Robb, M. A., Cheeseman, J. R., Montgomery, J. A., Vreven, J., Kudin, K. N., Burant, J. C., Millam, J. M., Iyengar, S. S., Tomasi, J., Barone, V., Mennucci, B., Cossi, M., Scalmani, G., Rega, N., Petersson, G. A., Nakatsuji, H., Hada, M., Ehara, M. P., Toyota, K., Fukuda, R., Hasegawa, J., Ishida,

M., Nakajima, T., Honda, Y., Kitao, O., Nakai, H., Klene, M., Li, X., Knox, J. E., Hratchian, H. P., Cross, J. B., Adamo, Jaramillo, J., Gomperts, R., Stratmann, R. E., Yazyev, O., Austin, A. J., Cammi, R., Pomelli, C., Ochterski, J. W., Ayala, P. Y., Morokuma, Voth, G. A., Salvador, P., Dannenberg, J. J., Zakrzewski, V. G., Dapprich, S., Daniels, A. D., Strain, M. C., Farkas, O., Malick, D. K., Rabuck, A. D., Raghavachari, K., Foresman, J. B., Ortiz, J. V., Cui, Q., Baboul, A. G., Clifford, S., Cioslowski, J., Stefanov, B. B., Liu, G., Liashenko, A., Piskorz, P., Komaromi, I., Martin, R. L., Fox, D. J., Keith, T., Al-Laham, M. A., Peng, C. Y., Nanayakkara, A., Challacombe, M., Gill, P. M. W., Johnson, B., Chen, W., Wong, M. W., Gonzalez, C., & Pople, J. A. (2005).

[39] Roy Dennington, Todd Keith and John Millam. (2009). *Semichem Inc.*, Shawnee Mission KS.

[40] Stash, A. I., & Tsirelson, V. G. Journal of Applied Crystallography, (2014). *47*, 2086-2089.

[41] Zhu, L. Y., Xu, D., Wang, X. Q., Liu, X. J., Zhang, G. H., & Sun, J. Crystal Research and Technology, 41(12), 1226–1230. (2006).

[42] Steiner T. Angewandte Chemie International Edition (2002). 41:48–76.

[43] Tristan Neumann, Gianpiero Gallo, Robert E. Dinnebier, and Christian Näther, Z. Anorg. Allg. Chem. 2020, 646, 88–94.

[44] E.M. Rakhmanko, Y.V. Matveichuk, V.V. Yasinetskii, J. Anal. Chem. (2015). 70, 178–185.

[45] JawherMakhlouf, ArtoValkonen, WajdaSmirani, Polyhedron. 213, 115625 (2022).

[46] J. Coates, in: R.A. Meyers (Ed), John Wiley and Sons Ltd, Chichester, 2000.

[47] S.J. Osborne, S. Wellens, C. Ward, S. Felton, R.M. Bowman, K.B. Binnemans,M. Swad_zba-Kwa_sny, H.Q.N. Gunaratne, P. Nockemann, Dalton Trans 44,11286–11289 (2015).

[48] Werner, J.; Rams, M.; Tomkowicz, Z.; Runˇcevski, T.; Dinnebier, R.E.; Suckert, S.; Näther, C. Thermodynamically metastable thiocyanato coordination polymer that shows slow relaxations of the magnetization. Inorg. Chem. 54, 2893–2901 (2015).

[49] Werner, J.; Runˇcevski, T.; Dinnebier, R.; Ebbinghaus, S.G.; Suckert, S.; Näther, C. Thiocyanato coordination polymers with isomeric coordination networks—Synthesis, structures, and magnetic properties. Eur. J. Inorg. Chem. 20, 3236–3245 (2015).

[50] Wöhlert, S.; Runˇcevski, T.; Dinnebier, R.E.; Ebbinghaus, S.G.; Näther, C. Synthesis, structures, polymorphism, and magnetic properties of transition metal thiocyanato coordination compounds. Cryst. Growth Des. 14, 1902–1913 (2014).

[51] M. Wriedt, C. Näther, Preparation of new ligand-deficient thiocyanato compounds with cooperative magnetic phenomena by thermal decomposition of their ligand-rich precursors, Eur. J. Inorg. Chem. 3201 (2010).

[52] Kakian, F. Abadi, M. S. S. Gholipour, A. Fadaie, M. Zamanzad, B. Khairi, S. Damavandi, M. S. Gene Reports, 100433. (2019).

[53] Sun, X. Gao, Y. Ding, Z. Zhao, Y. Yang, Y. Sun, Q. Zhang, J. International Journal of Biological Macromolecule, (2020).

[54] X.-Y. Meng, H.-X. Zhang, M. Mezei, M. Cui. Comput. Aided. Drug Des. 7 146–157(2011).

[55] S. Ahmad, S. Raza, R. Uddin, S.S. Azam. 77 72–85 (2017).

[56] V.N. Maiorov, G.M. Crippen, J. Mol. Biol. 235 625–634(1994).

[57] M.A. Alamri, M. ul Qamar, M.U. Mirza, R. Bhadane, S.M. Alqahtani, I. Muneer, Froeyen, O.M.H. Salo-Ahen, J.Biomol. Struct. Dyn. 1–13(2020).

[58] Fukui, K.. Role of frontier orbitals in chemical reactions. Science, 218, 747–754(1982).

[59] Zumdahl et al., University Science books, Sausalito, CA). (2000).